

# REPORT DOCUMENTATION PAGE

Public reporting burden for this collection of information is estimated to average 1 hour per response, including the time gathering and maintaining the data needed, and completing and reviewing the collection of information. Send comment this collection of information, including suggestions for reducing this burden to Washington Headquarters Services, Directorate for Information Operations and Reports, 1215 Jefferson Davis Highway, Suite 1204, Arlington, VA 22202-4302 and to the Office of Management and Budget, Paperwork Project, Washington, DC 20503.

AFRL-SR-AR-TR-05-

0342

1. AGENCY USE ONLY (Leave blank)		2. REPORT DATE 8-Aug-05	3. REPORT TYPE AND DATES COVERED Final Report August 1, 2004 to July 31, 2005
4. TITLE AND SUBTITLE AFOSR DURIP equipment grant: Scalable Shared Memory Supercomputer Replacement for DOD Research			5. FUNDING NUMBERS FA9550-04-1-0355
6. AUTHOR(S) J. V. Moloney			8. PERFORMING ORGANIZATION REPORT NUMBER
7. PERFORMING ORGANIZATION NAME(S) AND ADDRESS(ES) Department of Mathematics 617 N. Santa Rita Avenue University of Arizona Tucson, Arizona 85721			
9. SPONSORING / MONITORING AGENCY NAMES(S) AND ADDRESS(ES) Air Force Office of Scientific Research ATTN: Dr. Arje Nachman--NM 875 North Randolph Street, Suite 324, Rm. 3112 Arlington, Virginia 22203			10. SPONSORING/MONITORING AGENCY REPORT NUMBER
11. SUPPLEMENTARY NOTES			
12a. DISTRIBUTION/AVAILABILITY STATEMENT Approved for public release; distribution unlimited.			12b. DISTRIBUTION CODE
13. ABSTRACT (Maximum 200 words)  This instrumentation grant has enabled a dramatic enhancement in in-house supercomputing power at ACMS. The SGI ONYX2 22-processor system with 7 Gbytes of memory was replaced by the new SGI Altix 32-Itanium processor system with 64 Gbytes of memory. The combination of higher speed processor (factor of 6), higher interprocessor bandwidth and much larger accessible shared memory (64 Gbytes) has meant that problems that were previously inaccessible are now well within reach.			
14. SUBJECT TERMS			15. NUMBER OF PAGES 31
			16. PRICE CODE
17. SECURITY CLASSIFICATION OF REPORT UNCLASSIFIED	18. SECURITY CLASSIFICATION UNCLASSIFIED	19. SECURITY CLASSIFICATION OF ABSTRACT UNCLASSIFIED	20. LIMITATION OF ABSTRACT UL

**Final Report**  
**August 1 2004 to July 31, 2005**  
**FA9550-04-1-0355**

**AFOSR DURIP equipment grant:**  
**Scalable Shared Memory Supercomputer Replacement for DOD**  
**Research**

**Arizona Center for Mathematical Sciences**  
**Department of Mathematics**  
**University of Arizona**  
**PI: J.V. Moloney**

This instrumentation grant has enabled a dramatic enhancement in in-house supercomputing power at ACMS. The SGI ONYX2 22-processor system with 7 Gbytes of memory was replaced by the new SGI Altix 32-Itanium processor system with 64 Gbytes of memory. The combination of higher speed per processor (factor of 6), higher interprocessor bandwidth and much larger accessible shared memory (64 Gbytes) has meant that problems that were previously inaccessible are now well within reach. Moreover, this system offers an exciting upgrade path, initially to dual-core and eventually to multi-core (16) processors. This new capability, installed in July 2004, is already having a significant impact on the three AFOSR funded projects:

1. F496200210380    Novel Designs and Coupling Schemes for Affordable High Energy Laser Modules
2. F496200310194    Computational Nonlinear Optics: Femto Atmospheric Light String Applications
3. FA95500410213    Fundamental Modeling and Design Strategies in Computational Photonics: Applications to Lasercomm through clouds and Electro-optical/Nanophotonics

In addition, the added leverage provided by the purchase of the Altix system and a very generous trade-in value on the old ONYX2 system, enabled us to purchase a 21-node (42-CPU) AMD Opteron cluster with 84 Gbytes of memory. This cluster, which has a high speed Infiniband interconnection fabric, took some time to stabilize as it represented the first such cluster system integration attempt involving Silicon Graphics and Atipa engineers. The goal was to seamlessly integrate the Altix shared memory system with this mixed shared/distributed memory environment thereby offering unparalleled supercomputing performance. The full system integration involved three vendors: Silicon Graphics (SGI Altix), Atipa (Opteron Cluster) and Voltaire (infiniband interconnection fabric between Cluster nodes, fast local node Virtual Parallel 1 TB disk storage, 3 TB disk storage and the connection to the Altix). The fully integrated mixed supercomputing environment became available in July 2005 with the

**20050901 068**

installation of a ROCKS Redhat Linux queuing system. This integrated supercomputing laboratory is illustrated in the figure attached. We have just replaced 8 dual Opteron nodes on the cluster with 8 dual core, dual CPU modules. This has increased the number of available cluster CPUs further by 16 processors and moreover, provides 8 quad processor nodes for smaller scale shared memory computing.

**F496200210380      Novel Designs and Coupling Schemes for Affordable High Energy Laser Modules**

This MRI project has benefited greatly from the new supercomputing environment. Large scale simulations of double clad and micro-structured active fibers is now possible. Record powers with single frequency operation at eye-safe 1.5  $\mu\text{m}$  wavelength from centimeter long Er/Yb-doped phosphate glass doped fibers. New large core micro-structured phosphate fiber designs are currently being investigated as a pathway to further power scaling by shortening further the active fiber to achieve even greater longitudinal mode discrimination. The second project on power scaling of semiconductor VECSEL structures has received a major boost from the enhanced supercomputing performance afforded by the SGI and Cluster systems. Our unique closed-loop approach to designing such high power, high brightness laser systems requires supercomputing at many different levels. First, we need to optimize the semiconductor epi structure for operating laser active layer temperatures. This requires microscopically computing the semiconductor quantum well (QW) optical gain and refractive index spectra over the relevant physically accessible landscape of carrier density and temperature. These properties together with wafer-level photoluminescence spectra are proving invaluable in providing direct feedback to the semiconductor materials growers. Large scale simulation including optical and thermal transport in the semiconductor active mirror (sub-cavity), free-space propagation to the external passive mirror and full thermal transport through all heat-spreading and heat-sinking elements provides a major computational challenge. We currently have 2 versions of such a simulator working on our SGI shared memory machine: 1) A full scale simulation with coarse-grained time stepping –this provides a powerful tool for designing and optimizing the whole device and, 2) Treatment of the semiconductor active mirror+cooling elements as a lumped active mirror (with inputs provided from 1)) and a full spatio-temporal simulation of the transverse and longitudinal mode structure. The latter will allow us to optimize the active VECSEL for spectrally narrow, high brightness performance.

**F496200310194      Computational Nonlinear Optics: Femto Atmospheric Light String Applications**

The main effort here has been the development of ultra-fast, fully vectorial, vector Maxwell solvers for applications to the areas of atmospheric light string propagation, self-trapping of pulsed lasers in condensed media, white-light supercontinuum generation in bulk media and micro-structured fibers and nonlinear X-waves. These codes have been implemented in parallel on the SGI Altix machine and show excellent scaling to multiple CPUs. A significant number of papers have been published based on these solvers and utilizing the SGI compute engine. These have been documented in annual reports for this grant. A major new thrust of the research is to design more rigorous physical models for ultra-fast light-matter interaction and couple these to our unidirectional Maxwell and full Maxwell solvers. All computational aspects of these models

are extremely challenging and we are collaborating with different groups worldwide in search of computationally efficient but physically accurate computational models and schemes. We envisage taking advantage of our unique mixed shared/distributed memory computer architecture in tackling some of these emerging problems. All efforts here are particularly relevant to the emerging research field of extreme nonlinear optics. A manuscript, detailing the main theoretical developments of this work is attached.

**FA95500410213    Fundamental Modeling and Design Strategies in Computational Photonics: Applications to Lasercomm through clouds and Electro-optical/Nanophotonics**

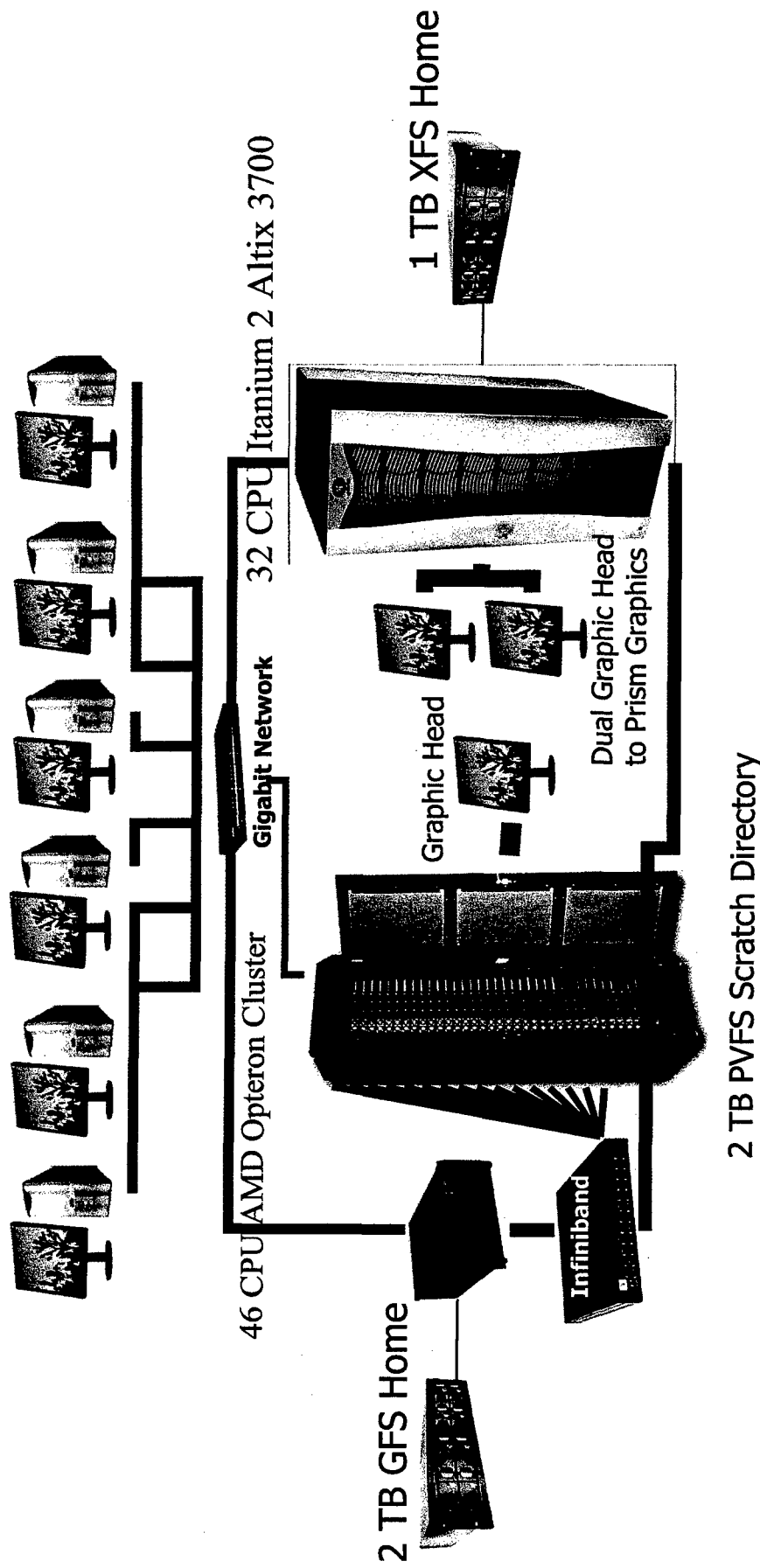
The main thrust of the initial phase of this effort has been in researching current state-of-the-art theoretical and computational methodologies with a view to exploiting our progress made under F496200210380 on the development of high power, high brightness, spectrally narrow VECSEL sources. Semiconductor wafers grown under the current project are designed from scratch by the ACMS research team. Currently we are exploring whether it is feasible to design partially-coherent lasercomm sources based on VECSEL arrays.

The computational nanophotonics effort relies heavily on the distributed memory cluster for 3D vector Maxwell simulation using our implementation of the FDTD time domain approach. Our working non-uniform mesh FDTD Maxwell solver is being employed to investigate light coupling from external sources into photonic crystal and nano-feature structures. We are also investigating the full 3D confined defect modes in 3D photonic crystals with a view to isolating the localized evanescent field from the propagating component. The role of surface plasmon modes in enhancing transmission through nanoscale holes in metallic films is also being studied. The dramatically increased throughput offered by our supercomputing facility has significantly enhanced our capability to solve new classes of computationally intensive problems.

# ACMS Photonics Supercomputing Laboratory

---

## Dual Opteron Workstations



# Full Vectorial, Intense Ultrashort Pulse Propagators: Derivation and Applications

J. V. Moloney and M. Kolesik

Arizona Center for Mathematical Sciences and Optical Sciences Center,  
University of Arizona, Tucson AZ 85721  
jml@acms.arizona.edu

## 1.1 Introduction

Rapid progress in recent years in the development of high power ultrashort pulse laser systems has opened up a whole new vista of applications and computational challenges. Amongst those applications that are most challenging from a computational point of view are those involving explosive critical self-focusing with concomitant explosive growth in the generated light spectrum. Moreover, new experimental developments in the field of extreme nonlinear optics will require more rigorous propagation models beyond those existing in the current literature. Specific applications areas chosen for illustration in this chapter include atmospheric light string propagation and, nonlinear self-trapping in condensed media. These examples exhibit rather different aspects of intense femtosecond pulse propagation and demonstrate the robustness and flexibility of the unidirectional Maxwell propagator. A novel aspect of our approach is that the pulse propagator is designed to faithfully capture the light-material interaction over the broad spectral landscape of relevance to the interaction. Moreover the model provides a seamless and physically self-consistent means of deriving the many ultrashort pulse propagation equations presented in the literature.

## 1.2 Derivation of Unidirectional Pulse Propagation Equations

### 1.2.1 Starting point: Maxwell Equations

In this Section we expand the discussion presented in [1]. We outline the key steps in deriving a physically self-consistent and robust ultrashort pulse propagator that resolves the underlying optical carrier wave while enabling propagation over many meter propagation lengths. Our goal is to retain the full rigor of Maxwell's equations while reducing the problem complexity by

constraining the model to unidirectional propagation. As our immediate interest is in very short intense pulse propagation with potentially large induced nonlinear polarization, we will need to accurately capture the very broad spectral landscape that the pulse experiences during its interaction with a host dielectric material. In many cases, spectral superbroadening is such that the generated bandwidth far exceeds in magnitude the underlying carrier frequency i.e  $\Delta\omega/\omega_0 \gg 1$ . In this limit, we expect the Nonlinear Schrödinger Equation (NLSE) to fail. Many attempts have been made to derive nonlinear envelope models that go beyond NLSE and we will discuss most of these below when we show explicitly how each can be seamlessly derived from our unidirectional pulse propagation equation (UPPE).

### Time-propagated and space-propagated equations

Most of the pulse propagation problems in nonlinear optics are solved in one of two formulations: Either one has an initial condition (electric and magnetic fields) specified in all space, and the evolution is calculated along the time axis, or the initial condition is given as a function of local pulse time and transverse (w.r.t. propagation direction) coordinates, and the numerical evolution proceeds along the propagation axis. We refer to these cases as time- and z-propagated equations.

The z-propagated approach is much more common in nonlinear optics simulations based on envelope equations, often related to NLS. The time-propagated approach is on the other hand common for solvers based on direct integration of Maxwell's equations.

Due to space limitations, we focus in this chapter on the z-UPPE. As discussed in [1] in more detail, the time-propagated versions of UPPE are more suitable for tight-focusing scenarios when non-paraxial effects start to play a role. The z-propagated equations are easier to use in situations that allow to neglect the longitudinal field components as sources of nonlinear material responses.

The z-propagated approach is more common in nonlinear optics and we start by deriving it explicitly, then discuss briefly its numerical implementation, relation to other envelope models and provide some illustrative examples of its implementation. We refer the reader to [1] for details concerning the details of numerical treatment of the nonlinear material response in both t-UPPE and z-UPPE cases.

#### 1.2.2 Starting point: Maxwell Equations

As a first step in derivation of various versions of UPPE, we derive an exact coupled-modes system of equations. This is a well-known textbook formula that can be found in the literature in several different forms. To keep our derivation self-contained, we re-derive the starting formula using a standard

approach based on orthogonality relations for modes of an electromagnetic field.

Electromagnetic fields of a light pulse propagating along the  $z$  axis can be expanded into modal contributions that reflect the geometry of the waveguide (we consider homogeneous medium a special case of the latter).

$$\begin{aligned} \mathbf{E}(x, y, z, t) &= \sum_{m, \omega} A_m(\omega, z) \mathcal{E}_m(\omega, x, y) e^{i\beta_m(\omega)z - i\omega t} \\ \mathbf{H}(x, y, z, t) &= \sum_{m, \omega} A_m(\omega, z) \mathcal{H}_m(\omega, x, y) e^{i\beta_m(\omega)z - i\omega t} \end{aligned} \quad (1.1)$$

Here,  $m$  labels all transverse modes, and an initial condition  $A_m(\omega, z = 0)$  is supposed to be given or calculated from the field values at  $z = 0$ . Note that the above expansion is valid for the transverse components only.

To save space, the following short-hand notation will be used below

$$\begin{aligned} \mathcal{E}_m &\equiv \mathcal{E}_m(\omega, x, y) e^{i\beta_m(\omega)z - i\omega t} \\ \mathcal{H}_m &\equiv \mathcal{H}_m(\omega, x, y) e^{i\beta_m(\omega)z - i\omega t} . \end{aligned} \quad (1.2)$$

The starting point is Maxwell's equations. We consider a non-magnetic medium ( $\mu = \mu_0$ ) with a linear permittivity  $\epsilon(\omega, x, y)$  that doesn't depend on the propagation coordinate  $z$ .

$$\begin{aligned} \mathbf{j} + \partial_t \mathbf{P} + \epsilon_0 \partial_t \epsilon * \mathbf{E} &= \nabla \times \mathbf{H} \\ -\mu_0 \partial_t \mathbf{H} &= \nabla \times \mathbf{E} \end{aligned} \quad (1.3)$$

where the star represents a convolution.

First, we scalar-multiply the Maxwell's equations by the complex conjugate modal fields

$$\begin{aligned} \mathcal{E}_m^* \cdot (\mathbf{j} + \partial_t \mathbf{P}) + \epsilon_0 \mathcal{E}_m^* \cdot \partial_t \epsilon * \mathbf{E} &= \mathcal{E}_m^* \cdot \nabla \times \mathbf{H} \\ -\mu_0 \mathcal{H}_m^* \cdot \partial_t \mathbf{H} &= \mathcal{H}_m^* \cdot \nabla \times \mathbf{E} . \end{aligned} \quad (1.4)$$

Using the formula  $\mathbf{b} \cdot (\nabla \times \mathbf{a}) = \nabla \cdot (\mathbf{a} \times \mathbf{b}) + \mathbf{a} \cdot (\nabla \times \mathbf{b})$ , we transform both RHS to obtain

$$\begin{aligned} \mathcal{E}_m^* \cdot (\mathbf{j} + \partial_t \mathbf{P}) + \epsilon_0 \mathcal{E}_m^* \cdot \partial_t \epsilon * \mathbf{E} &= \nabla \cdot [\mathbf{H} \times \mathcal{E}_m^*] + \mathcal{H}_m^* \cdot [\nabla \times \mathcal{E}_m^*] \\ -\mu_0 \mathcal{H}_m^* \cdot \partial_t \mathbf{H} &= \nabla \cdot [\mathbf{E} \times \mathcal{H}_m^*] + \mathcal{E}_m^* \cdot [\nabla \times \mathcal{H}_m^*] . \end{aligned} \quad (1.5)$$

Since modal fields themselves satisfy the Maxwell's equations

$$\begin{aligned} \nabla \times \mathcal{E}_m^* &= -\mu_0 \partial_t \mathcal{H}_m^* \\ \nabla \times \mathcal{H}_m^* &= \epsilon_0 \partial_t \epsilon * \mathcal{E}_m^* , \end{aligned} \quad (1.6)$$

the above equations can be written as

$$\begin{aligned} \mathcal{E}_m^* \cdot (\mathbf{j} + \partial_t \mathbf{P}) + \epsilon_0 \mathcal{E}_m^* \cdot \partial_t \epsilon * \mathbf{E} &= \nabla \cdot [\mathbf{H} \times \mathcal{E}_m^*] - \mu_0 \mathcal{H}_m^* \cdot \partial_t \mathcal{H}_m^* \\ -\mu_0 \mathcal{H}_m^* \cdot \partial_t \mathbf{H} &= \nabla \cdot [\mathbf{E} \times \mathcal{H}_m^*] + \epsilon_0 \mathcal{E}_m^* \cdot \partial_t \epsilon * \mathcal{E}_m^* \end{aligned} \quad (1.7)$$



We subtract the two equations and collect terms that constitute full time derivatives

$$\mathcal{E}_m^* \cdot (\mathbf{j} + \partial_t \mathbf{P}) + \partial_t [\epsilon_0 \mathcal{E}_m^* \cdot \epsilon * \mathbf{E}] = \nabla \cdot [\mathbf{H} \times \mathcal{E}_m^*] - \partial_t [\mu_0 \mathcal{H}_m^* \cdot \mathbf{H}] - \nabla \cdot [\mathbf{E} \times \mathcal{H}_m^*]. \quad (1.8)$$

Now integrate over the whole  $xyt$  domain. Note that all terms except the first and the  $\partial_z$  (implicit in  $\nabla \cdot$ ) are derivatives that give rise to “surface terms” after integration over  $x, y, t$ . Since we consider spatially and temporally localized pulse-like solutions, these terms vanish. The only surviving derivative will be  $\partial_z$  from  $\nabla \cdot$ :

$$\int \mathcal{E}_m^* \cdot (\mathbf{j} + \partial_t \mathbf{P}) dx dy dt = \partial_z \int \mathbf{z} \cdot [\mathbf{H} \times \mathcal{E}_m^*] dx dy dt - \partial_z \int \mathbf{z} \cdot [\mathbf{E} \times \mathcal{H}_m^*] dx dy dt \quad (1.9)$$

Here and in what follows,  $t$  integrations are understood like this:  $\int dt \equiv \frac{1}{T} \int_{-T/2}^{+T/2} dt$  where  $T$  is a large normalization “volume,” and integrals over  $x, y$  are understood in a similar way. Because only transverse field components enter above equation, we can use our modal expansion here:

$$\begin{aligned} & \int \mathcal{E}_m^* \cdot (\mathbf{j} + \partial_t \mathbf{P}) dx dy dt = \\ & \partial_z \int \mathbf{z} \cdot [\sum_{n,\Omega} A_n(\Omega, z) \mathcal{H}_n(\Omega) \times \mathcal{E}_m^*(\omega)] e^{i\beta_n(\Omega)z - i\Omega t} e^{-i\beta_m(\omega)z + i\omega t} dx dy dt \\ & - \partial_z \int \mathbf{z} \cdot [\sum_{n,\Omega} A_n(\Omega, z) \mathcal{E}_n(\Omega) \times \mathcal{H}_m^*(\omega)] e^{i\beta_n(\Omega)z - i\Omega t} e^{-i\beta_m(\omega)z + i\omega t} dx dy dt. \end{aligned} \quad (1.10)$$

Integration over time gives a Kronecker delta between angular frequencies,  $\delta_{\Omega\omega}$ , which in turn reduces the sum over  $\Omega$ :

$$\begin{aligned} & \int \mathcal{E}_m^* \cdot (\mathbf{j} + \partial_t \mathbf{P}) dx dy dt = \\ & \partial_z \int \mathbf{z} \cdot [\sum_n A_n(\omega, z) \mathcal{H}_n(\omega, x, y) \times \mathcal{E}_m^*(\omega, x, y)] e^{i\beta_n(\omega)z} e^{-i\beta_m(\omega)z} dx dy \\ & - \partial_z \int \mathbf{z} \cdot [\sum_n A_n(\omega, z) \mathcal{E}_n(\omega, x, y) \times \mathcal{H}_m^*(\omega, x, y)] e^{i\beta_n(\omega)z} e^{-i\beta_m(\omega)z} dx dy. \end{aligned} \quad (1.11)$$

Collecting like terms results in an equation

$$\begin{aligned} & \int \mathcal{E}_m^* \cdot (\mathbf{j} + \partial_t \mathbf{P}) dx dy dt = \partial_z \sum_n A_n(\omega, z) e^{i\beta_n(\omega)z} e^{-i\beta_m(\omega)z} \times \\ & \int \mathbf{z} \cdot [\mathcal{H}_n(\omega, x, y) \times \mathcal{E}_m^*(\omega, x, y) - \mathcal{E}_n(\omega, x, y) \times \mathcal{H}_m^*(\omega, x, y)] dx dy. \end{aligned} \quad (1.12)$$

where the general orthogonality relation

$$\int \mathbf{z} \cdot [\mathcal{E}_m \times \mathcal{H}_n^* - \mathcal{H}_m \times \mathcal{E}_n^*] dx dy = 2\delta_{m,n} N_m(\omega) \quad (1.13)$$

can be used to reduce the sum over modes

$$\int \mathcal{E}_m^* \cdot (\mathbf{j} + \partial_t \mathbf{P}) dx dy dt = -\partial_z \sum_n A_n(\omega, z) e^{i\beta_n(\omega)z} e^{-i\beta_m(\omega)z} 2\delta_{m,n} N_m(\omega), \quad (1.14)$$

and finally obtain the evolution equation for the expansion coefficients:

$$\partial_z A_m(\omega, z) = -\frac{1}{2N_m(\omega)XYT} \int_{-T/2}^{+T/2} dt \int_{-Y/2}^{+Y/2} dy \int_{-X/2}^{+X/2} dx \times \\ e^{-i\beta_m(\omega)z+i\omega t} \mathcal{E}_m^*(\omega, x, y) \cdot [j(x, y, t) + \partial_t \mathbf{P}(x, y, t)] \quad (1.15)$$

This is the starting point for the z-propagated unidirectional equations.

### 1.2.3 Z-propagator UPPE for homogeneous medium

In the following, Eq. (1.15) is specialized for the case of a homogeneous medium. Field modes are plane waves labeled by transverse wavenumbers  $k_x, k_y$ , a polarization index  $s = 1, 2$ , and a  $\pm$  sign depending on the direction of propagation along  $z$ :

$$m \equiv k_x, k_y, s, \pm. \quad (1.16)$$

The frequency and wavenumber dependent propagation “constant” is

$$\beta_{k_x, k_y, s, \pm}(\omega) \equiv k_z(\omega, k_x, k_y) = \sqrt{\omega^2 \epsilon(\omega)/c^2 - k_x^2 - k_y^2}, \quad (1.17)$$

and the modal field amplitudes are

$$\mathcal{E}_{k_x, k_y, s, \pm} = \mathbf{e}_s \exp[ik_x x + ik_y y \pm ik_z(\omega, k_x, k_y)z] \quad (1.18)$$

$$\mathcal{H}_{k_x, k_y, s, \pm} = \frac{1}{\mu_0 \omega} \mathbf{k} \times \mathcal{E}_{k_x, k_y, s, \pm}. \quad (1.19)$$

Here,  $\mathbf{e}_{s=1,2}$  are unit polarization vectors normal to the wave-vector

$$\mathbf{k} = \{k_x, k_y, k_z \equiv \sqrt{\omega^2 \epsilon(\omega)/c^2 - k_x^2 - k_y^2}\}. \quad (1.20)$$

From these formulas, it is straightforward to calculate the modal normalization constant

$$2N_{k_x, k_y, s, \pm}(\omega) = \int z \cdot [\mathcal{E}_m \times \mathcal{H}_m^* - \mathcal{H}_m \times \mathcal{E}_m^*] dx dy = \\ 2z \cdot [\mathbf{e}_s \times (\mathbf{k} \times \mathbf{e}_s)] \frac{1}{\mu_0 \omega} = \pm 2k_z(\omega, k_x, k_y) \frac{1}{\mu_0 \omega} \quad (1.21)$$

$$N_{k_x, k_y, s, \pm}(\omega) = \pm \frac{k_z(\omega, k_x, k_y)}{\mu_0 \omega}. \quad (1.22)$$

Now we can insert expressions for the modal fields and normalization constant into coupled mode equation Eq. (1.15)

$$\partial_z A_{k_x, k_y, s, \pm}(\omega, z) = -\frac{\omega \mu_0}{2k_z} e^{-ik_z z} \int \frac{dx dy dt}{L_x L_y T} e^{i(\omega t - k_x x - k_y y)} \times \\ \mathbf{e}_s \cdot [j(x, y, z, t) + \partial_t \mathbf{P}(x, y, z, t)] \quad (1.23)$$

The above integral is nothing but spatial and temporal Fourier transform, so one can write it in the spectral domain as

$$\partial_z A_{k_x, k_y, s, +}(\omega, z) = \frac{\omega}{2\epsilon_0 c^2 k_z} e^{-ik_z z} e_s \cdot [i\omega P_{k_x, k_y}(\omega, z) - j_{k_x, k_y}(\omega, z)] \quad (1.24)$$

This is the propagation equation that is actually solved numerically, but let us express it in terms of field rather than in terms of modal expansion coefficients. From a modal expansion, the transverse part of the electric field is

$$\mathbf{E}_{k_x, k_y, +}^\perp(\omega, z) = \sum_{s=1,2} e_s^\perp A_{k_x, k_y, s, +}(\omega, z) e^{ik_z(k_x, k_y, \omega)z}, \quad (1.25)$$

and its  $z$  derivative reads

$$\partial_z \mathbf{E}_{k_x, k_y, +}^\perp(\omega, z) = ik_z(k_x, k_y, \omega) \mathbf{E}_{k_x, k_y, +}^\perp(\omega, z) + \sum_{s=1,2} e_s^\perp \partial_z A_{k_x, k_y, s, +}(\omega, z) e^{ik_z(k_x, k_y, \omega)z} \quad (1.26)$$

Using Eq. (1.24) we obtain the homogeneous medium full-vectorial UPPE

$$\begin{aligned} \partial_z \mathbf{E}_{k_x, k_y, +}^\perp(\omega, z) &= ik_z \mathbf{E}_{k_x, k_y, +}^\perp(\omega, z) + \\ &\sum_{s=1,2} e_s^\perp e_s \cdot \left[ \frac{i\omega^2}{2\epsilon_0 c^2 k_z} \mathbf{P}_{k_x, k_y}(\omega, z) - \frac{\omega}{2\epsilon_0 c^2 k_z} \mathbf{j}_{k_x, k_y}(\omega, z) \right] \end{aligned} \quad (1.27)$$

This is an exact system of equations that describes the evolution of modal amplitudes along the  $z$ -axis for the forward propagating field. A similar equation holds for the backward propagating component, of course.

Because the nonlinear polarization in this equation results as a response to the *complete* field, this equation can't be used to calculate the forward field only. The equation becomes "unidirectional" only after resorting to the following approximation

$$\mathbf{P}(\mathbf{E}), \mathbf{j}(\mathbf{E}) \rightarrow \mathbf{P}(\mathbf{E}_f), \mathbf{j}(\mathbf{E}_f) \quad (1.28)$$

In other words, to obtain a closed system to solve numerically, we must require that the nonlinear polarization is well approximated by the nonlinear polarization calculated only from the forward propagating field. This means that the equation is only applicable when the back-reflected portion of the field is so small that its contribution to the nonlinearity can be neglected.

#### 1.2.4 Z-propagated UPPE, simplified, most practical version

Eq. 1.27, with nonlinear polarization approximated by Eq. 1.28 can easily become a rather large system to solve numerically for typical problems encountered in the femtosecond pulse propagation area. Fortunately, in most cases

the transverse dimensions of the resulting field remain relatively large compare to the wavelength, and further approximations are possible. Concretely, one can neglect the  $z$  components of the field and polarization vectors. In such a situation the sum over polarization vectors reduces approximately to unity

$$\sum_{s=1,2} \mathbf{e}_s^\perp \mathbf{e}_s \approx 1, \quad (1.29)$$

and the full UPPE simplifies into an equation for the transverse component(s) of the field

$$\begin{aligned} \partial_z E_{k_x, k_y}(\omega, z) &= ik_z E_{k_x, k_y}(\omega, z) + \frac{i\omega^2}{2\epsilon_0 c^2 k_z} P_{k_x, k_y}(\omega, z) - \frac{\omega}{2\epsilon_0 c^2 k_z} j_{k_x, k_y}(\omega, z), \\ k_z &= \sqrt{\omega^2 \epsilon(\omega)/c^2 - k_x^2 - k_y^2}. \end{aligned} \quad (1.30)$$

This is the most useful form for practical calculation, and is therefore called simply UPPE in the following.

### 1.2.5 Nonlinear material response

In most cases, the propagation equations discussed in this chapter do not require a specific form of material response. However, for the sake of concreteness, as well as for discussion of numerical methods, we want to describe a generic model of nonlinear material response. We consider a nonmagnetic, dispersive medium with relative permittivity  $\epsilon$  that is a function of the transverse coordinates  $x, y$  and of the angular frequency  $\omega$

$$\epsilon = \epsilon(\omega, x, y), \quad \mu = \mu_0. \quad (1.31)$$

This medium specification includes any dispersive homogeneous medium such as air or water as well as structured fiber-like media such as photonic, microstructured and tapered optical fibers.

Nonlinear effects are usually described in terms of polarization  $P$  through the material constitutive relation:

$$\mathbf{D} = \epsilon_0 \epsilon * \mathbf{E} + \mathbf{P}. \quad (1.32)$$

The star in this formula represents a convolution integral with  $\epsilon$  being the linear response function corresponding to the frequency dependent  $\epsilon(\omega, x, y)$ . The non-linear polarization is an "arbitrary" function of the electric field  $\mathbf{P} = \mathbf{P}(\mathbf{E})$ . We will also include a current density that is driven by the optical field

$$\mathbf{j} = \mathbf{j}(\mathbf{E}) \quad (1.33)$$

to describe interactions with plasma generated by the high-intensity optical pulse.

The main physical effects that influence propagation of ultrashort, high-power light pulses in nonlinear dispersive media include the optical Kerr and stimulated Raman effects, free-electron generation, defocusing by the generated plasma and losses caused by avalanche and multiphoton ionization (MPI). With minor modifications, models including these effects can be used for description of ultra-short optical pulses propagation in gases [2–18], condensed bulk media [19–23] and in conventional, microstructured, and tapered fibers [24–26] as well as in ultra-thin silica “wires” [27].

The optical Kerr and stimulated Raman effects cause a local modification of the optical susceptibility

$$\mathbf{P} = \epsilon_0 \Delta\chi \mathbf{E} \quad (1.34)$$

that responds to the history of the light intensity  $I$ :

$$\Delta\chi = 2n_b n_2 \left[ (1-f)I + f \int_0^\infty \mathcal{R}(\tau) I(t-\tau) d\tau \right] \quad (1.35)$$

Here,  $f$  is the fraction of the delayed nonlinear response, and  $\mathcal{R}$  is the memory function of the stimulated Raman effect. Parameterization by  $\mathcal{R}(\tau) \sim \sin(\Omega\tau)e^{-\Gamma\tau}$  is often sufficient for ultrashort pulses [28]. This simple formula has the advantage of easy implementation that avoids explicit calculation of the convolution integral. Often, an even simpler, exponential memory function is used,  $\mathcal{R}(\tau) \sim e^{-\Gamma\tau}$  in simulations (see e.g. [29]). If the real memory function is sufficiently complex, a numerical convolution approach must be used to calculate the convolution. This is e.g. the case in silica [30].

Of course, E. 1.34 neglects the dependence of the Kerr effect on wavelength. Although  $\Delta\chi$  may exhibit a finite memory due to the Raman contribution, it acts on the instantaneous value of  $\mathbf{E}$  only. This is in part due to only rather limited data available on frequency dependence of the nonlinear coefficients  $n_2$  (see Ref. [31] for silica), but it also simplifies practical calculations considerably. Consequently, the “background” index of refraction  $n_b$  can be approximated by a constant value taken at the central frequency of the initial pulse.

Because of the potentially high intensities occurring in femtosecond pulses, free electrons are generated by MPI and avalanche mechanisms. Then it is necessary to account for the response of the optical field to the presence of a dilute plasma. Since the relevant times scales are so short, plasma diffusion and ion motion are neglected, and the free-electron density  $\rho$  is usually obtained as a solution to an equation of the following form [12, 13, 28]

$$\partial_t \rho = aI\rho + b(I) - c\rho^2. \quad (1.36)$$

Here,  $I$  is the light intensity,  $a$  parameterizes the avalanche free-electron generation, and  $b(I)$  represents the Multi Photon Ionization (MPI) rate that is a highly nonlinear function of the intensity. The last term describes plasma recombination.

We assume that the collective electron velocity  $\mathbf{v}$  responds to the optical field and the total current density is governed by the following simple equation (see e.g. Ref. [32])

$$\frac{d}{dt}\mathbf{j}(t) = \frac{e^2}{m_e}\rho(t)\mathbf{E}(t) - \mathbf{j}(t)/\tau_c \quad (1.37)$$

where  $\tau_c$  is the mean time between collisions experienced by electrons. This equation is solved together with (1.36) to capture effects of the plasma on the propagation of the optical field, namely defocusing due to plasma and plasma induced losses.

Losses caused by multiphoton ionization are usually incorporated as either an equivalent current (see e.g [32, 33]) or an imaginary susceptibility contribution that extracts from the field the energy needed for the free-electron generation.

### 1.2.6 Numerical algorithms

The general structure of both t- and z-UPPE propagation equations is quite similar. A UPPE equation actually comprises a large system of ordinary differential equation with a free propagation part, and a nonlinear coupling.

An important feature that affects the numerical solution strategy is that these equations are written in the spectral space, either in the three dimensional space of wave-vectors (t-propagated UPPE) or in a two-dimensional space of transverse wave-vectors plus a one dimensional angular-frequency space (z-propagated UPPE). At the same time, the nonlinear material response must be calculated in the real-space representation. Consequently, a good implementation of Fast Fourier Transform is essential for a UPPE solver.

Due to the nature of FFT, or spectral transforms in general, parallelization of the solver is more suited to a shared memory architecture than to the Message Passing Interface approach. Further, since the most time-consuming portion of the code deals with calculating the RHS of the equation, we choose to apply a single threaded library for ODE solvers (gsl in our case) and only parallelize the calculation of derivatives needed in the ODE solver.

For concreteness, we describe solution of the z-propagated UPPE equation:

$$\begin{aligned} \partial_z E_{k_x, k_y}(\omega, z) &= ik_z E_{k_x, k_y}(\omega, z) + \frac{i\omega^2}{2\epsilon_0 c^2 k_z} P_{k_x, k_y}(\omega, z) - \frac{\omega}{2\epsilon_0 c^2 k_z} j_{k_x, k_y}(\omega, z), \\ k_z &= \sqrt{\omega^2 \epsilon(\omega)/c^2 - k_x^2 - k_y^2}. \end{aligned} \quad (1.38)$$

Suppose we have a solution at  $z = 0$ , and want to propagate it over a distance corresponding to an integration step  $\Delta z$ . Although we wrote the equation in terms of field, it is more natural to solve numerically for the modal expansion coefficients to eliminate fast oscillatory terms. We therefore express the field through the expansion coefficients  $A$  which are actually the “native solver variables:”

$$E_{k_x, k_y}(\omega, z) = A_{k_x, k_y}(\omega, z) e^{ik_z(\omega, k_x, k_y)z} \quad (1.39)$$

to transform the equation into

$$\partial_z A_{k_x, k_y}(\omega, z) = e^{-ik_z z} \left[ + \frac{i\omega^2}{2\epsilon_0 c^2 k_z} P_{k_x, k_y}(\omega, z) - \frac{\omega}{2\epsilon_0 c^2 k_z} j_{k_x, k_y}(\omega, z) \right] \quad (1.40)$$

Depending on the concrete ODE scheme one chooses to use, the ODE solver may require one to calculate the derivative (RHS) at various values of  $z$ . Non-linear polarization and current are of course functions of the electric field which in turn is calculated for any given  $z$  from (1.39). That is nothing but applying a linear propagator (in the spectral representation) to a given field. Thus, to evaluate the RHS in (1.40) given  $A_{k_x, k_y}(\omega, z)$ , one first applies (1.39) to obtain electric field in the spectral-space representation. Subsequently, a real-space representation is obtained by Fourier transform. (Note that this is a “global” operation which forces each parallel execution thread to access large amount of data “owned” by all other threads. This is the main reason why the UPPE solvers are easier to implement on a shared memory machine.) Having the electric field in real space, one calculates the material response using the model described in the previous Section. This is done by integrating the material equations along the time dimension independently for each point in the transverse  $x, y$  plane. Consequently, this portion of the code is straightforward to parallelize. As a result, one obtains the nonlinear polarization and current in the real-space representation. This is then Fourier transformed back into spectral space to finally evaluate the RHS in the propagation equation (1.40). An ODE solver calls this procedure as many times as it needs to perform a single integration step and thus calculates  $A_{k_x, k_y}(\omega, z + \Delta z)$ .

A final operation that finishes one solver step is to calculate the field in the frame moving with an appropriate group velocity so that the pulse is kept in the center of the computational domain. This is achieved by applying a modified linear propagator

$$A_{k_x, k_y}(\omega, z + \Delta z) \rightarrow A_{k_x, k_y}(\omega, z + \Delta z) \exp\left\{i\left[k_z(\omega, k_x, k_y) - \frac{\omega - \omega_R}{v_g}\right]\Delta z\right\} \quad (1.41)$$

The group velocity that enters above is usually calculated from the linear dispersion relation

$$\frac{1}{v_g} = \partial_\omega k_z(\omega, k_x = 0, k_y = 0)|_{\omega=\omega_R} \quad (1.42)$$

at the frequency that corresponds to the maximum of the pulse spectral power (pulse center frequency). Let us emphasize that this last operation is just a change of coordinates, so the introduction of the reference frequency at this point doesn't change the light propagation in any way. However, it is important to include the moving frame, because it makes it easier and more efficient to apply absorbing boundary layers in the computational domain.

Without a moving window, the computational domain would be periodically wrapped into itself in the time direction. In order to apply artificial absorption at the boundary and also for integrating the material equations, the latter would need to be identified at each step.

Thus, since the UPPE is actually a big ODE system, the solver implementation is simple in principle, though it involves significant “auxiliary” calculations described above to supply the ODE solver with the routine to calculate the derivatives.

A final remark in this Section concerns axially symmetric problems. We usually treat these in radial coordinates and apply a numerical Hankel transform instead of the Fourier transform. This is a “slow” transform with a dense matrix, but due to the relatively small computational domain radially symmetric problems require, this is not a big problem. Alternatively, one could treat such situations by finite differencing in the radial dimension, but it would mean accepting additional (paraxial) approximation, and would introduce artificial numerical dispersion into the algorithm.

### 1.3 General method for derivation of various propagation equations from UPPE

Several types of unidirectional propagation equation are widely used in the nonlinear optics literature. The most important examples are Non-Linear Schrödinger (NLS) equation [34], Nonlinear Envelope Equation [35] (NEE), the First-Order Propagation equation [33] (FOP), Forward Maxwell’s equation [36] (FME), and several other equations that are closely related to these. The derivations found in the literature differ from equation to equation, and in some cases the physical meaning of the required approximations may not be readily evident due to a number of neglected terms.

In this section, we provide a unified approach that will subsequently be used to derive several of the light-pulse propagation equations found in the literature. The main benefit of re-deriving known equations from a common starting point, namely UPPE, using the same method, is that it allows us to compare the physical assumptions and approximation underlying different equations. It also reveals relations between the equation which may not be obvious either because of their apparently different form, or because of different methods used in the original derivations.

It is instructive to break the derivation procedure into several steps. As a first step, we adopt a scalar, one component approximation and write the UPPE in the following form:

$$\partial_z E_{k_x, k_y}(\omega, z) = iK E_{k_x, k_y}(\omega, z) + iQ P_{k_x, k_y}(\omega, z) \quad (1.43)$$

where

$$K(k_x, k_y, \omega) = \sqrt{\omega^2 \epsilon(\omega)/c^2 - k_x^2 - k_y^2} \quad (1.44)$$



is the linear field propagator in the spectral representation, and

$$Q(k_x, k_y, \omega) = \frac{\omega^2}{2\epsilon_0 c^2 \sqrt{\omega^2 \epsilon(\omega)/c^2 - k_x^2 - k_y^2}} \quad (1.45)$$

will be called nonlinear coupling term.

In the second step, we replace  $K$  and  $Q$  by suitable approximations. In most cases they are nothing but Taylor expansions in frequency and in transverse wavenumbers.

To obtain envelope equations, one expresses the field in terms of an envelope by factoring out the carrier wave at a chosen reference angular frequency  $\omega_R$  with the corresponding wave-vector  $k_R = K(0, 0, \omega_R)$ :

$$E(x, y, z, t) = \mathcal{A}(x, y, z, t) e^{i(k_R z - \omega_R t)} \quad (1.46)$$

A similar factorization is of course introduced for the nonlinear polarization  $P(x, y, z, t)$  as well.

Step three consist in transforming the equation from the spectral- to the real-space representation. Mathematically, this is nothing but a Fourier transform that results in the following standard rules for differential operators:

$$(\omega - \omega_R) \rightarrow i\partial_t \quad ik_x \rightarrow \partial_x \quad ik_y \rightarrow \partial_y \quad \partial_z \rightarrow ik(\omega_R) + \partial_z \quad (1.47)$$

Finally, in most cases we also transform to a frame moving with a suitable group velocity such that the pulse remains close to the center of the computational domain.

### 1.3.1 Derivation of Non-Linear Schrödinger Equation from UPPE

The Nonlinear Schrödinger Equation (see [34] for applications in optics) (NLS) is a prototype propagation equation in nonlinear optics. This is also the simplest case suitable to illustrate the general procedure outlined above. One characteristic feature of NLS and of other envelope type equations is the presence of a reference frequency. Usually, one chooses the reference angular frequency  $\omega_R$  as the central frequency of the initial pulse, but this is not necessary. Actually it is useful to keep in mind that  $\omega_R$  is to a certain extent a free parameter, and that the obtained results must be almost independent of its concrete choice. If a numerical simulation turns out to be sensitive to the choice of  $\omega_R$ , it means that an envelope equation is being used outside of its region of validity.

Following the general procedure, we replace the  $K$  and  $Q$  “coefficients” with appropriate approximations. We denote by  $k_R = k(\omega_R)$  the reference wavenumber corresponding to the chosen reference frequency  $\omega_R$ , and take

$$K(k_x, k_y, \omega) = \sqrt{\omega^2 \epsilon(\omega)/c^2 - k_x^2 - k_y^2}$$

$$\approx k_R + v_g^{-1}(\omega - \omega_R) + \frac{k''}{2}(\omega - \omega_R)^2 - \frac{1}{2k_R}(k_x^2 + k_y^2) \quad (1.48)$$

This is a second-order Taylor expansion in  $\omega - \omega_R$  and in  $k_x, k_y$ .

In the nonlinear coupling coefficient, we neglect all variable dependencies and take its value at the reference frequency and zero transverse wavenumbers:

$$Q(k_x, k_y, \omega) = \frac{\omega^2}{2\epsilon_0 c^2 \sqrt{\omega^2 \epsilon(\omega)/c^2 - k_x^2 - k_y^2}} \approx \frac{\omega_R}{2\epsilon_0 n(\omega_R) c} \quad (1.49)$$

For simplicity, in NLS we only account for the instantaneous optical Kerr effect, and write the nonlinear polarization envelope as

$$\mathcal{P} = 2\epsilon_0 n(\omega_R) n_2 I \mathcal{A} \quad (1.50)$$

Inserting the above expressions into (1.43, 1.46) we obtain

$$\partial_z \mathcal{A} = +i v_g^{-1}(\omega - \omega_R) \mathcal{A} + \frac{i k''}{2}(\omega - \omega_R)^2 \mathcal{A} - \frac{i}{2k_R}(k_x^2 + k_y^2) \mathcal{A} + \frac{i \omega_R}{c} n_2 I \mathcal{A} \quad (1.51)$$

It is customary to normalize the envelope amplitude such that  $|\mathcal{A}|^2 = I$ . Using rules (1.47) we finally obtain the NLS equation:

$$(\partial_z + v_g^{-1} \partial_t) \mathcal{A} = \frac{i}{2k_R} \Delta_{\perp} \mathcal{A} - \frac{i k''}{2} \partial_{tt} \mathcal{A} + \frac{i \omega_R}{c} n_2 |\mathcal{A}|^2 \mathcal{A} \quad (1.52)$$

The above derivation shows explicitly what approximations need to be adopted to obtain NLS: Approximating  $K$  to second order in frequency and transverse wavenumber amounts to the paraxial, and quasi-monochromatic approximations for the linear wave propagation. The approximation in the nonlinear coupling  $Q$  also requires a narrow spectrum in order to be able to represent  $Q$  by a constant.

### 1.3.2 Nonlinear Envelope Equation

The Nonlinear Envelope Equation [35] is a paraxial equation with some additional approximations related to chromatic dispersion. This equation appears to be extremely close to the paraxial version of UPPE.

Once again we follow the general procedure and approximate the linear propagator by its paraxial version:

$$K(k_x, k_y, \omega) = \sqrt{\omega^2 \epsilon(\omega)/c^2 - k_x^2 - k_y^2} \approx +k(\omega) - \frac{c}{2\omega n_b(\omega_R)}(k_x^2 + k_y^2) \quad (1.53)$$

This is essentially the second-order (paraxial) Taylor expansion in transverse wavenumbers with only minor additional approximation. Namely, we replaced

$n_b(\omega) \rightarrow n_b(\omega_R)$  in the denominator of the diffraction term, and thus partly neglected the chromatic dispersion.

Further, the first term in the above approximation, which is an exact propagation constant for a plane wave propagating along the  $z$  axis, is re-expressed as a sum of its two lowest-order Taylor expansion terms plus the rest:

$$k(\omega) = k(\omega_R) + v_g^{-1}(\omega - \omega_R) + D(\omega - \omega_R) \quad (1.54)$$

where

$$D(\omega - \omega_R) = \sum_{n=2}^{\infty} \left( \frac{\partial^n k}{\partial \omega^n} \right)_{\omega=\omega_R} \frac{(\omega - \omega_R)^n}{n!} \quad (1.55)$$

This is formally exact and can be practically implemented in the spectral domain without further approximations, but sometimes a finite number of series expansion terms is used to fit the linear chromatic dispersion of a medium or of a waveguide. What we understand under NEE in the following assumes an exact treatment of the dispersion operator.

Next, we approximate the nonlinear coupling term. Unlike in NLS, we preserve the frequency dependence exactly, but neglect the transverse wave-number dependence:

$$Q(k_x, k_y, \omega) \equiv \frac{\omega^2}{2\epsilon_0 c^2 \sqrt{\omega^2 \epsilon(\omega)/c^2 - k_x^2 - k_y^2}} \approx \frac{(\omega - \omega_R) + \omega_R}{2\epsilon_0 c n(\omega_R)} \quad (1.56)$$

Here, as in the free propagation term, we neglect the chromatic dispersion of the background index of refraction.

After putting the above approximations for  $K$  and  $Q$  into the original UPPE, we obtain

$$\begin{aligned} \partial_z \mathcal{A} = & i v_g^{-1}(\omega - \omega_R) \mathcal{A} + i D(\omega - \omega_R) \mathcal{A} \\ & - \frac{ic}{2\omega_R n(\omega_R)} \left(1 + \frac{\omega - \omega_R}{\omega_R}\right)^{-1} (k_x^2 + k_y^2) \mathcal{A} \\ & + \frac{i\omega_R}{2\epsilon_0 c n(\omega_R)} \left(1 + \frac{\omega - \omega_R}{\omega_R}\right) \mathcal{P} \end{aligned} \quad (1.57)$$

Finally, transforming into the real-space representation, we arrive at NEE

$$\partial_z \mathcal{A} + v_g^{-1} \partial_t \mathcal{A} = i D(i \partial_t) \mathcal{A} + \frac{i}{2k_R} \left(1 + \frac{i}{\omega_R} \partial_t\right)^{-1} \Delta_{\perp} \mathcal{A} + \frac{ik_R}{2\epsilon_0 n_b^2(\omega_R)} \left(1 + \frac{i}{\omega_R} \partial_t\right) \mathcal{P} \quad (1.58)$$

Thus, the additional approximations underlying the NEE are paraxiality both in the free propagator and in the nonlinear coupling, and a small error in the chromatic dispersion introduced when the background index of refraction is replaced by a constant, frequency independent value in both the spatio-temporal correction term and in the nonlinear coupling term. Note that the latter approximations are usually not serious at all.

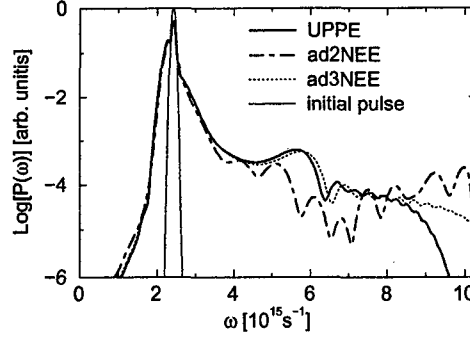


**Fig. 1.1.** Supercontinuum generated in a femtosecond pulse propagating in air. Full curve was obtained from the full UPPE simulation while the other curves correspond to NEE equation simulated with two and three terms included in the dispersion operator.

As in all envelope equations a reference frequency and a reference wave-number appear in the NEE. They are chosen equal to the central frequency and wave-number of the input pulse in practical calculation, but one has to keep in mind that these quantities are artificial and to a certain degree arbitrary “gauge” parameters that, of course, do not appear in the Maxwell’s equations. Consequently, numerical solutions should not depend on how the reference is chosen. In other words a propagation equations should be “reference-frequency-invariant.” While NLS is manifestly dependent on the reference choice, NEE is nearly invariant although  $\omega_R$  appears in it several times. For example, the spatio-temporal focusing correction term (operator)  $\omega_R^{-1}(1 + \frac{1}{\omega_R}\partial_t)^{-1}$  that appears in the NEE equation and modifies the diffraction term seems to depend on the reference  $\omega_R$ , but it is in fact proportional to  $\omega^{-1}$  as long as it is implemented in the spectral domain that allows to include all orders of the series expansion. It is to be stressed that this (approximate) invariance is only achieved in the infinite order. Truncating the operators that appear in the NEE to finite number of series expansion terms breaks the invariance and brings about undesirable artifacts as we point out in the following example.

We consider a 25-femtosecond (0.1mm waist) pulse with a carrier wavelength of 775 nm and power of 8GW propagating in air. The pulse duration is chosen very short to highlight propagation effects that are absent in the NLS approach, namely space-time focusing and the frequency dependent nonlinear response (shock formation). We compare supercontinuum generation using UPPE with full chromatic dispersion of dry air taken into account in the wavelength region from 1200 to 200 nm [37] and the NEE equation with the dispersion operator  $\mathcal{D} = \sum_{k=2}^L \beta^{(k)}/k!(i\partial_t)^k$  (Eqn. (??)) is expanded up to the second ( $L = 2$ ) and/or third ( $L = 3$ ) order with  $\beta^{(k)}$  being purely real in

this case. We term the latter approximations ad2NEE and ad3NEE, respectively (standing for NEE with approximate dispersion). In all cases we assume an instantaneous optical Kerr effect with  $n_2 = 5 \times 10^{-23} \text{m}^2/\text{W}$ , and plasma generation by multiphoton ionization. The reader is referred to Ref. [28] for a physical description of the model.

Figure 1.1 shows the pulse spectrum after the self-focusing collapse is arrested by plasma generation. In all cases, a broad high-frequency component is generated on the steepened trailing edge of the pulse as described previously in Ref. [38]. However the details of the spectra are rather different. Here, the UPPE solution describes the correct propagation properties of all wavelengths that contribute to the spectral range shown. The difference between the UPPE and ad2(3)NEE solutions can be traced to difference in the susceptibility they model. It happens that the GVD is rather small around 800 nm and the approximated susceptibility rapidly deviates from the actual susceptibility at higher frequencies. Including the third-order dispersion substantially improves the agreement with the UPPE solution. The remaining discrepancy is then restricted to the high-frequency range in which the supercontinuum spectral intensity falls-off. This demonstrates that in the NEE the dispersion operator should be treated exactly in the spectral domain or care should be exercised in approximating chromatic dispersion by an expansion. When the dispersion is handled properly, NEE is an excellent approximation. It can be shown that the error it introduces is of fourth order in the transverse wave-number.

### 1.3.3 Partially corrected NLS

The Partially Corrected NLS (PC-NLS) equation can be viewed as a “simplification” of NEE. It is derived from the UPPE in the same way, with one additional step. Namely, the following first order series expansion is applied in the correction term of the free propagator in Eqn.(1.57):

$$(1 + \frac{\omega - \omega_R}{\omega_R})^{-1} \approx (1 - \frac{\omega - \omega_R}{\omega_R}) \quad (1.59)$$

This step is meant to make it easy to implement a numerical solver in the real space, as it results in the equation that only contains “simple” differential operators in the real-space representation:

$$\partial_z \mathcal{A} + v_g^{-1} \partial_t \mathcal{A} = iD(i\partial_t) \mathcal{A} + \frac{i}{2k_R} (1 - \frac{i}{\omega_R} \partial_t) \Delta_{\perp} \mathcal{A} + \frac{ik_R}{2\epsilon_0 n_b^2(\omega_R)} (1 + \frac{i}{\omega_R} \partial_t) \mathcal{P} \quad (1.60)$$

While it may seem that the Partially Corrected NLS is essentially NEE with a “little more” approximation, this equation is not to be recommended. Because of the arbitrary truncation of an infinite series, the dispersion properties of the linear part of this equation are unphysical. While the PC-NLS provides better-than-NLS approximation around the reference frequency  $\omega_R$ , its dispersion properties become rather pathological around  $\omega \approx 2\omega_R$  where

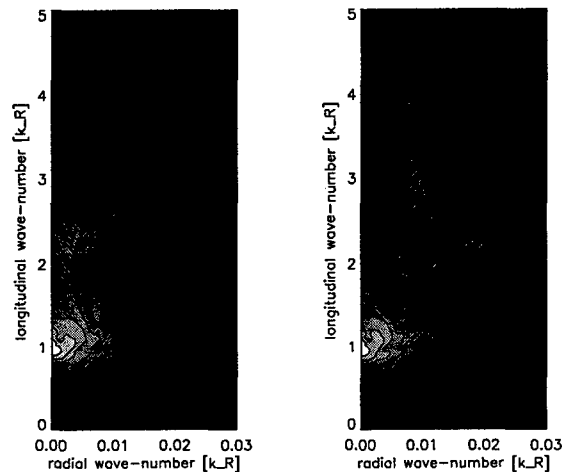


**Fig. 1.2.** Spatial spectra of a supercontinuum generated in air. Left panel represents a solution obtained from UPPE, the right panels is a corresponding spectrum obtained from PCNLS. Artifacts in the spectrum around the wavenumbers that correspond to the twice the reference frequency are clearly visible.

its diffraction term changes sign as a consequence of the truncated correction factor. Artifacts in the angular distribution of the spectrum can be observed at high frequencies beyond  $\omega \approx 2\omega_R$ . This is illustrated in Fig. 1.2. Consequently, this equation is only applicable in the same regime as the NLS, namely when the spectrum of the pulse remains relatively narrow.

## 1.4 Applications of UPPE simulators

This section provides three illustrative applications of the z-UPPE model. The first is the computationally more challenging as it involves a full 3D + time simulation of the propagation of a wide pancake shaped pulse in air. The second provides a nice illustration of the need to go beyond the paraxial approximation for nonlinear X-wave generation in condensed media and the last illustrates the subtle interplay between plasma generation and chromatic dispersion in limiting the extent of the supercontinuum spectrum.

### 1.4.1 Femtosecond Atmospheric Light Strings

#### Multiple filament formation

This application of the z-UPPE simulator illustrates break-up of a high-power, wide femtosecond pulse into chaotically interacting light filaments. Beams that

carry power exceeding the critical self-focusing power many times usually break transversally into multiple filaments. To capture such dynamics, a fully spatially resolved simulator is needed that doesn't impose axial symmetry.

Below, we illustrate how such multiple filaments are concurrently created at different transverse and longitudinal locations, and how they interact with the low-intensity background. It was first proposed in [15] that such an interaction is crucial for long distance propagation of high-power femtosecond pulses in air. The basic idea is that of dynamic exchange of energy between multiple, essentially unsynchronized and spatially sharply localized filament cores and the low-intensity, spatially wide pedestal of the beam.

In this wide-beam simulation, the initial condition is a Gaussian pulse with a phase perturbation. The waist of the initially collimated Gaussian was chosen to be 5mm, the pulse duration is 500 fs,  $\lambda = 248\text{nm}$ , and the maximal intensity is  $2 \times 10^{14}\text{Wm}^{-2}$ . The total pulse energy is approximately 9mJ. A random phase perturbation is imposed on the pulse to initiate the transverse break-up of the pulse into multiple filaments (see 1.3:). We adjusted the amplitude of the perturbation such that it results in the filamentation onset after a few meters of propagation.

The first stage of nonlinear self-focusing is driven by the smooth, large-scale profile of the pulse. After a few meters, local perturbations develop into hot spots which grow into high-intensity filaments. The first panel shows the overall scale of the input pulse with the high-intensity regions forming from the low-intensity background. There is practically no plasma formation at this propagation distance.

The initial perturbations grow rapidly and reach intensities high enough to ionize air (second panel). Collapse of a filament is eventually regularized by plasma induced defocusing. That causes decay of the filament and returns most of its energy into the low-intensity background. From there, new filaments grow and these replenishment cycles repeat with relatively modest energy losses to plasma generation (subsequent panels).

Later in the propagation, filaments start to appear in the peripheral regions further from the center. This is due to less overall intensity and therefore slower self-focusing and growth of perturbations. Though it is not evident on these fluence pictures, later-stage filaments tend to generate less plasma than the ones that appear at the very beginning of the filamentation onset. This is the stage when the single-filament dynamic spatial replenishment scenario crosses over to a regime where replenishment energy originates in "neighboring" filaments rather than from the same one.

This gradual change in the dynamics is reflected also in the plasma generation as shown in Fig. 1.4 Initial sharp spikes in the total number of generated electrons, associated with the onset of individual filaments, decay with distance. We expect the shot-to-shot fluctuation to smooth-out the sharp features of this curve due to randomization of the filament formation. The late-stage filaments are less "organized" than those created just after the self-focusing onset. Consequently, it takes less of the plasma generation to arrest their col-

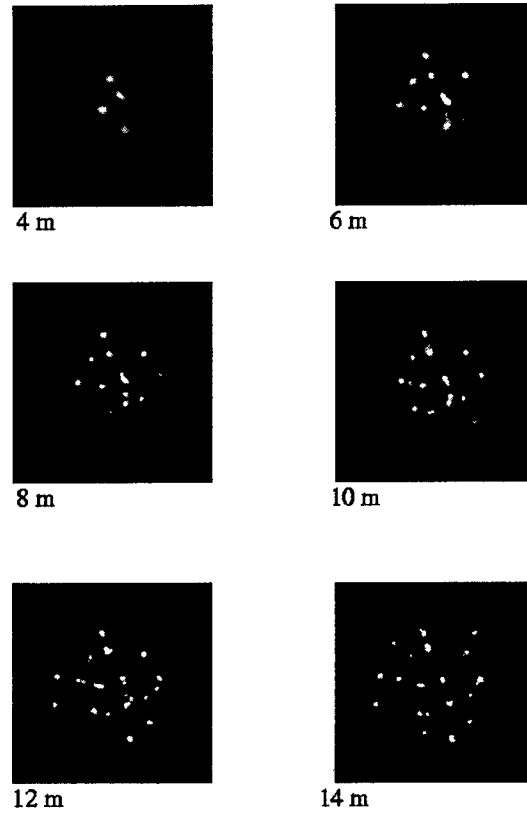


**Fig. 1.3.** Transverse profile of the fluence (time-integrated intensity) “measured” at several propagation distances. The color scheme was chosen such that one can see the structure of the low-intensity background. On the other hand, it makes it difficult to compare filament intensities. The size of the depicted domain in all panels is  $1\text{cm} \times 1\text{cm}$ .

lapse. One can say that the increasing “disorder” in the developing composite pulse makes the collapse arrest due to plasma more efficient and thus contributes to the ability of the pulse to propagate over long distances. One can speculate, and recent experiments indicate that a regime can be eventually reached where the plasma generation is almost negligible.



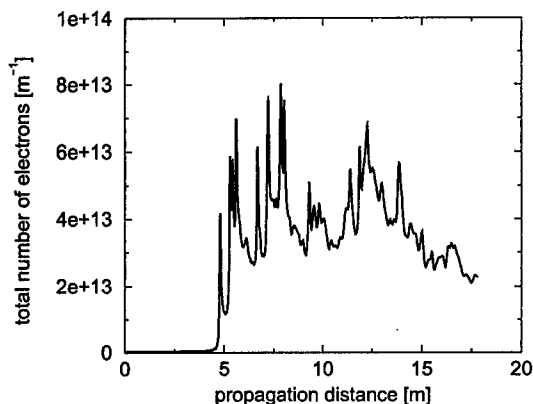


Fig. 1.4. Total number of free electrons generated as a function of propagation distance.

#### 1.4.2 Nonlinear X-waves in Condensed Media

In this Section, we present an example of simulation of an ultrashort pulse in water. This particular example requires that the solver captures correctly the linear dispersion in a broad range of frequencies and propagation angles, and is thus an ideal candidate for UPPE application. Full details can be found in an earlier publication [39]

We consider a loosely focused femtosecond pulse centered around the 520 nm wavelength, propagating in a water sample. An appropriate combination of focusing and pulse intensity and duration results in a long (compared to the Rayleigh range corresponding to the transverse size of the beam at the water-cell entrance).

Figure 1.5 shows the resulting filament transverse dimension (size) for several pulse energies as a function of the propagation distance in water (left). The right panel illustrates that supercontinuum is easily generated at these energies. We thus deal with a highly non-NLS regime.

The question we want to shed light on in this numerical experiment is what mechanism is responsible for creation of that seemingly several centimeters long filament. Further, we want to know if the mechanism is universal in any way.

First, it is important to note that what is actually observed, in experiment and in simulation alike, is not a “steady-state” self-guided filament. Rather, we deal with a series of pulse splitting events akin to the scenario of spatial dynamical replenishment [7]. In this case, however, the role of plasma as the arrestor of the self-focusing collapse is less pronounced compared to propagation in air.

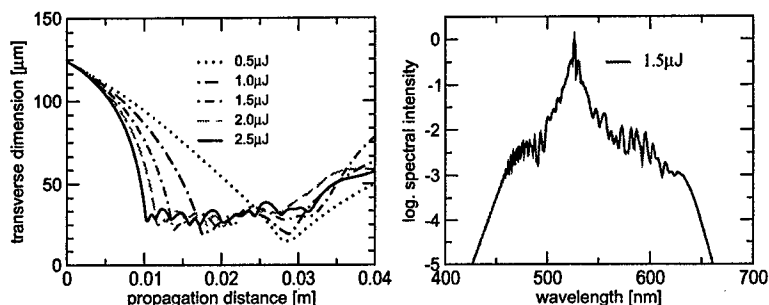


**Fig. 1.5.** Femtosecond pulse loosely focused into water creates a long filament with a nearly constant diameter that extends over many Rayleigh ranges (left), and generates a broad supercontinuum spectrum (right). This seemingly stationary filament is created by a series of very dynamic multiple pulse splittings illustrated in the following.

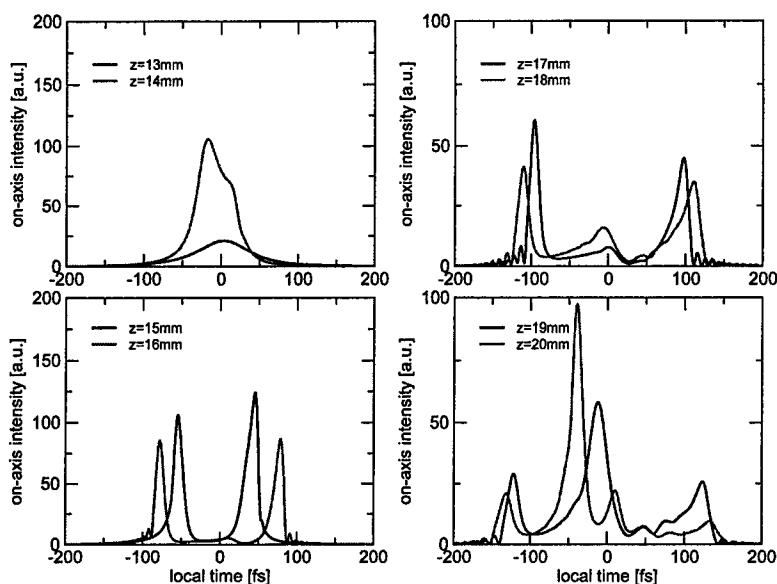


**Fig. 1.6.** Pulse splitting cycle: Single central pulse undergoes splitting. The split-off-pulses act a “scatterers,” which concentrate most of the energy in the spatio-temporal spectrum around loci that support “diffractionless” wave-forms. This provides the energy for a new central pulse, and the cycle repeats. . .

Figure 1.6 shows a series of snapshots that depict the temporal profile of on-axis intensity of the now quite complicated “pulse.” One observes several cycles consisting of formation and subsequent splitting of a sub-pulse in the center of the time domain. The “daughter” sub-pulses resulting from each

pulse-split event play an important role in the formation of the spatial and temporal spectrum. Namely they are still intense enough to induce localized changes to the material susceptibility that in turn follow these split-off pulses and thus propagate with different “group” velocities. These material waves then act as scatterers in a three-wave mixing process that transforms the input optical waves into scattered ones. Linear propagation dispersion properties together with the propagation velocity of the material wave then determine where in the spectral space will the scattered energy accumulate.

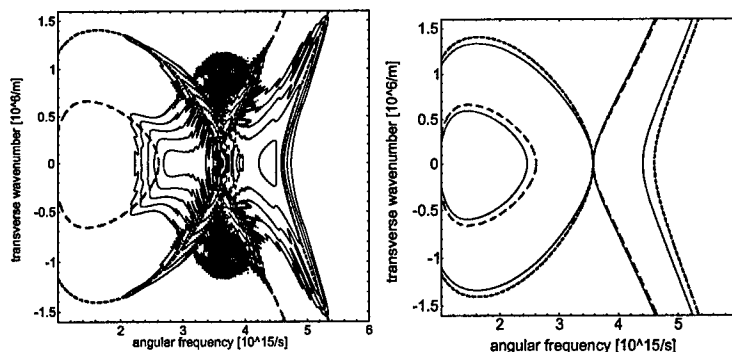


**Fig. 1.7.** Angle-resolved spectrum of an ultrashort pulse propagating in water (left panel). The dashed lines represent the loci of spectral energy concentration predicted from an effective three-wave mixing argument. The right panel compares these loci to the manifold that supports the spectrum of z-invariant X-wave solutions that propagate without distortions.

The resulting spatio-temporal spectrum of a loosely focused ultrashort pulse after propagation in water is shown in Fig. 1.7 on left. The dashed lines (in both, left and right panels) represent the loci where energy concentrates due to the non-linear interactions irrespectively of the details of the underlying dynamics. The resulting central X-shaped feature is always close to the manifold (shown in full line, right panel) that supports the z-invariant X-waves that propagate long distances without changing their spatio-temporal shapes. In any normal-GVD medium, the “theoretical X-wave” spectrum and the “real-pulse” spectral concentration will be close to each other because of the simple landscape of chromatic dispersion in the space of frequency and transverse wavenumber. Thus, even highly non-stationary pulses inherit their tendency for long-distance propagation from the nonlinear X-waves.

### 1.4.3 Supercontinuum Genration in Bulk Media

In this Section, we describe comparative simulations that provided further insight into how supercontinuum is generated by powerful femtosecond pulses

propagating in bulk medium. Readers interested in more details can found those in [22] and in [21]

The SC generation requires high intensities that are initiated by self-focusing collapse in the medium. The mechanism that arrests the collapse is supplied by multi-photon ionization (MPI) which produces both a direct energy loss for the collapsing field and an electron-ion plasma, which subsequently absorbs, defocuses, and spectrally blue-shifts the optical field. The combined effects of MPI and plasma defocusing provide a mechanism for the arrest of self-focusing collapse, which clamps the maximum intensity  $I_{max}$  reached by the collapsing pulse, and also limits the maximum rate of plasma generation  $\partial_t \rho \propto I_{max}^K$ , with  $\rho$  the plasma density and  $K$  the order of the MPI. The standard scenario [23, 40–43] maintains that the dominant contribution to spectral broadening comes from the spectral blue-shifting due to the plasma [42, 44], with the maximum blue-side frequency shift  $\Delta\omega_{max} \propto \partial_t \rho \propto I_{max}^K$ . Thus, according to the standard scenario, limiting of the maximum intensity  $I_{max}$  as self-focusing is arrested is the dominant factor that determines the spectral extent  $\Delta\omega_{max}$  of SC generation.

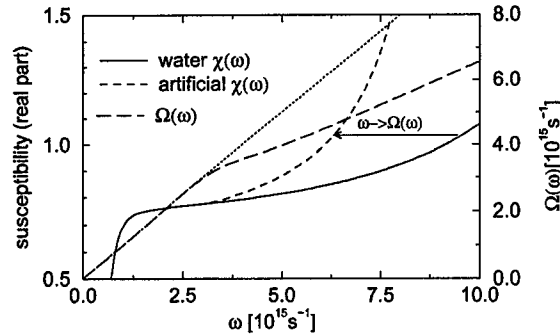


**Fig. 1.8.** “Artificial” vs “real” water susceptibility used in comparative simulations designed to test the standard supercontinuum generation scenario for bulk media.

In order to put the standard SC generation scenario to a test, we compare the water SC generation simulations with analogous simulations performed using an artificial medium which is the same as the “original” but with a modified linear dispersion. The latter is “constructed” such that the artificial medium exhibits self-focusing and plasma dynamics that are almost identical to those of the real medium model.

Frequency mapping  $\omega \rightarrow \Omega(\omega)$  is used to construct the artificial water susceptibility is shown in long-dashed line in Fig. 1.8 (the dotted line shows identity function for comparison). The artificial and water susceptibility functions are depicted in dashed and full lines, respectively in Fig. 1.8. The arrow

illustrates the susceptibility transformation. Susceptibility is preserved around the pulse carrier frequency, in order to preserve all the quantities that control the SC generation under the standard scenario, such as the highest light intensities and plasma density. Consequently, according to the standard scenario, the two media should generate the same SC spectra. Numerical simulations are used to check if this is the case.

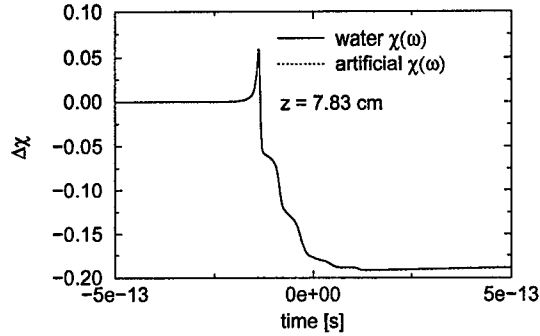


**Fig. 1.9.** Local susceptibility variation induced by the nonlinear effects in the femtosecond pulse. Water and a the comparative artificial medium exhibit very similar responses.

To show that both model media should indeed provide essentially the same SC spectrum in our simulations, provided the standard SC scenario is correct, we present a comparison of the nonlinear response for water and the artificial medium in Fig. 1.9. The nonlinear response consist in a local change  $\Delta\chi$  of the medium susceptibility. As a function of the “local time” at pulse location, it first increases due to the increasing intensity created by the selffocusing. Then the susceptibility change decrease into negative values because of the defocusing caused by the plasma generated in the high-intensity light pulse. The picture shows, that the nonlinear response of the artificial medium is extremely close to that of the water. This indicates that if the standard model of SC generation is complete, the almost same response dynamics implies closely similar SC spectra.

The comparison of the SC spectra obtained using the realistic and artificial water susceptibilities is shown in Fig. 1.10. The original and artificial medium spectra agree quite well in the vicinity of the excitation wavelength. However, at high frequencies the two materials produce drastically different continua. The dashed line shows the SC spectrum transformed by the same transformation that produced the artificial medium susceptibility from the water susceptibility. This appears to be very close to the artificial medium spectrum. This indicates that the extend of the spectrum is actually determined mostly by the linear dispersion properties of the medium.

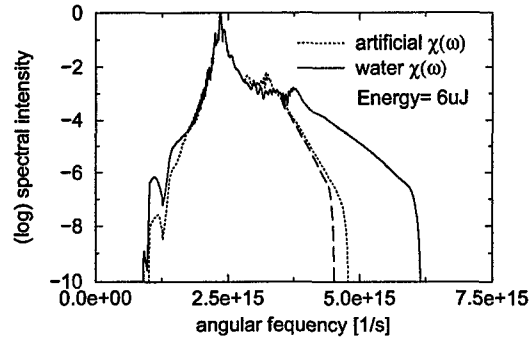


**Fig. 1.10.** Supercontinuum spectra generated in water and in the artificial medium. Dashed line represents the spectrum edge obtained from the real water spectrum the same way as the artificial susceptibility was obtained from the original water susceptibility. The standard SC scenario predicts the same spectra for both models.

Thus, we arrive at the conclusion that the standard scenario for supercontinuum generation in bulk media *is incomplete*. Although it correctly identifies the key quantities (peak intensity, plasma density generation rate) and processes (collapse arrest, MPI), our numerical experiments demonstrate that it doesn't explain the supercontinuum spectral properties.

To complete the supercontinuum generation picture for bulk media, the medium's linear susceptibility, as a function of frequency, must be taken into account as a key factor that determines the maximal attainable width of the white light spectrum.

Further simulations (not shown) also showed that the so-called supercontinuum band-gap dependence is due to stronger chromatic dispersion at higher frequencies. Namely, increasing the excitation frequency has a similar effect on the SC spectrum as the artificial modification of the susceptibility we used in our simulations; The curvature of the dispersion function is stronger closer to the band-gap and reduces the spectral broadening due to the larger phase-mismatch in the underlying wave mixing processes.

## 1.5 Future Work and Perspectives

This chapter has focused on procedures for deriving ultra short propagation pulse propagation models starting from Maxwell's equations. The unidirectional pulse propagation equation (UPPE) possesses all of the essential ingredients for current and future studies in the emerging field of extreme non-linear optics. We have shown that the latter provides a unifying theoretical framework from which the many propagation equations in the literature can be seamlessly derived. Moreover, the physical approximations made in these models are clearly exposed and their interrelationships stressed.

## 1.6 Acknowledgements

The authors would like to thank Ewan Wright of the College of Optical Sciences, University of Arizona for his continued active involvement and encouragement during the course of the work outlined in this chapter. One of the authors (JVM) is particularly indebted to Dr. Arje Nachman of the U.S Air Force Office of Scientific Research (AFOSR) for his continued support of this work. The authors wish to acknowledge funding support from the Air Force Office of Scientific Research under grants: AFOSR F49620-02-1-0194 and AFOSR F49620-02-1-0355.

## References

1. M. Kolesik and J. V. Moloney, Phys. Rev. E **70**, 036604 (2004).
2. A. Braun *et al.*, Opt. Lett. **20**, 73 (1995).
3. A. Brodeur *et al.*, Opt. Lett. **22**, 304 (1997).
4. H. R. Lange *et al.*, Opt. Lett. **23**, 120 (1998).
5. E. T. J. Nibbering *et al.*, Opt. Lett. **21**, 62 (1996).
6. O. G. Kosareva *et al.*, Opt. Lett. **22**, 1332 (1997).
7. M. Mlejnek, E. M. Wright, and J. V. Moloney, Opt. Lett. **23**, 382 (1998).
8. B. La Fontaine *et al.*, Phys. of Plasmas **6**, 1615 (1999).
9. M. Mlejnek, E. M. Wright, and J. V. Moloney, Phys. Rev. E **58**, 4903 (1998).
10. J. Schwartz *et al.*, Opt. Commun. **180**, 383 (2000).
11. A. Chiron *et al.*, Eur. Phys. J. D **6**, 383 (1999).
12. A. Couairon and L. Bergé, Phys. of Plasmas **7**, 193 (2000).
13. L. Bergé and A. Couairon, Phys. of Plasmas **7**, 210 (2000).
14. S. Petit, A. Talebpour, A. Proulx, and S. L. Chin, Opt. Commun. **175**, 323 (2000).
15. M. Mlejnek, M. Kolesik, J. V. Moloney, and E. M. Wright, Phys. Rev. Lett. **83**, 2938 (1999).
16. A. Talebpour, S. Petit, and S. L. Chin, Opt. Commun. **171**, 285 (1999).
17. J. V. Moloney, M. Kolesik, M. Mlejnek, and E. M. Wright, Chaos **10**, 559 (2000).
18. N. Aközbek, C. M. Bowden, A. Talebpour, and S. L. Chin, Phys. Rev. E **61**, 4540 (2000).
19. J. Noack and A. Vogel, IEEE J. Quantum Electron. **35**, 1156 (1999).
20. S. Tzortzakis *et al.*, Phys. Rev. Lett. **87**, 213902 (2001).
21. M. Kolesik, G. Katona, J. V. Moloney, and E. M. Wright, Phys. Rev. Lett. **91**, 043905 (2003).
22. M. Kolesik, G. Katona, J. V. Moloney, and E. M. Wright, Appl. Phys. B **77**, 185 (2003).
23. W. Liu *et al.*, Opt. Commun. **202**, 189 (2002).
24. J. M. Dudley and S. Coen, Opt. Lett. **27**, 1180 (2002).
25. J. M. Dudley *et al.*, J. Opt. Soc. Am. B **19**, 765 (2002).
26. A. L. Gaeta, Opt. Lett. **27**, 924 (2002).
27. L. Tong *et al.*, Nature **426**, 816 (2003).
28. M. Mlejnek, E. M. Wright, and J. V. Moloney, Opt. Lett. **23**, 382 (1998).
29. C. A. and B. L., Phys. Rev. Lett. **88**, 135003 (2002).

30. D. Hollenbeck and C. D. Cantrell, J. Opt. Soc. Am. B **19**, 2886 (2002).
31. D. Milam, Appl. Opt. **37**, 546 (1998).
32. V. P. Kandidov *et al.*, Appl. Phys. B **77**, 149 (2003).
33. M. Geissler *et al.*, Phys. Rev. Lett. **83**, 2930 (1999).
34. A. C. Newell and J. V. Moloney, *Nonlinear optics* (Addison-Wesley, Redwood City, CA, 1992).
35. T. Brabec and F. Krausz, Phys. Rev. Lett. **78**, 3282 (1997).
36. A. V. Husakou and J. Herrmann, Phys. Rev. Lett. **87**, 203901 (2001).
37. E. R. Peck and K. Reeder, J. Opt. Soc. Am. **62**, 958 (1972).
38. A. L. Gaeta, Phys. Rev. Lett. **84**, 3582 (2000).
39. M. Kolesik, E. M. Wright, and J. V. Moloney, Phys. Rev. Lett. **92**, 253901 (2004).
40. W. Lee Smith, P. Liu, and N. Bloembergen, Phys. Rev. A **15**, 2396 (1977).
41. A. Brodeur and S. L. Chin, Phys. Rev. Lett. **80**, 4406 (1998).
42. A. Brodeur and S. L. Chin, J. Opt. Soc. Am. B **16**, 637 (1999).
43. C. Nagura *et al.*, Appl. Opt. **41**, 3735 (2002).
44. Y.-D. Qin, D.-L. Wang, S.-F. Wang, and Q.-H. Gong, Chin. Phys. Lett. **18**, 390 (2001).